Clouds and the Earth's Radiant Energy System (CERES)

Algorithm Theoretical Basis Document

Empirical Estimates of Shortwave and Longwave Surface Radiation Budget Involving CERES Measurements

(Subsystem 4.6.0)

B. R. Barkstrom[1]
D. P. Kratz[1]
R. D. Cess[2]
Z. Li[3]
A. K. Inamdar[4]
V. Ramanathan[4]
S. K. Gupta[5]

[1]Atmospheric Sciences Division, NASA Langley Research Center, Hampton, Virginia 23681-0001
[2]Institute for Terrestrial and Planetary Atmospheres, Marine Sciences Research Center, State University of New York at Stony Brook, Stony Brook, New York 11794-5000
[3]Canada Centre for Remote Sensing, Ottawa, Ontario, Canada K1A0Y7
[4]Center for Clouds, Chemistry, and Climate, Scripps Institution of Oceanography, University of California at San Diego, La Jolla, California 92093
[5]Analytical Services & Materials, Inc., Hampton, Virginia 23666

June 2, 1997

CERES Top Level Data Flow Diagram

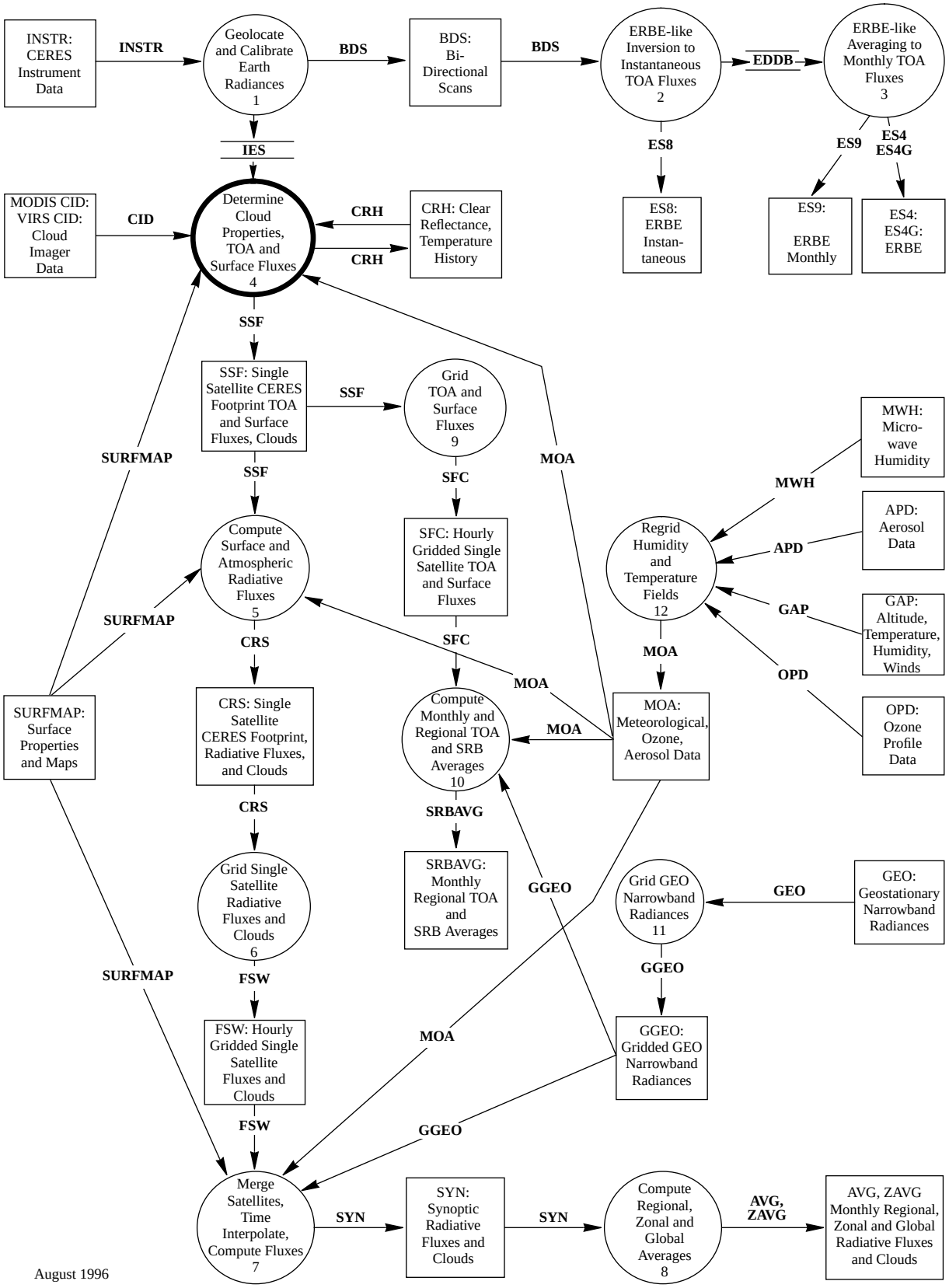

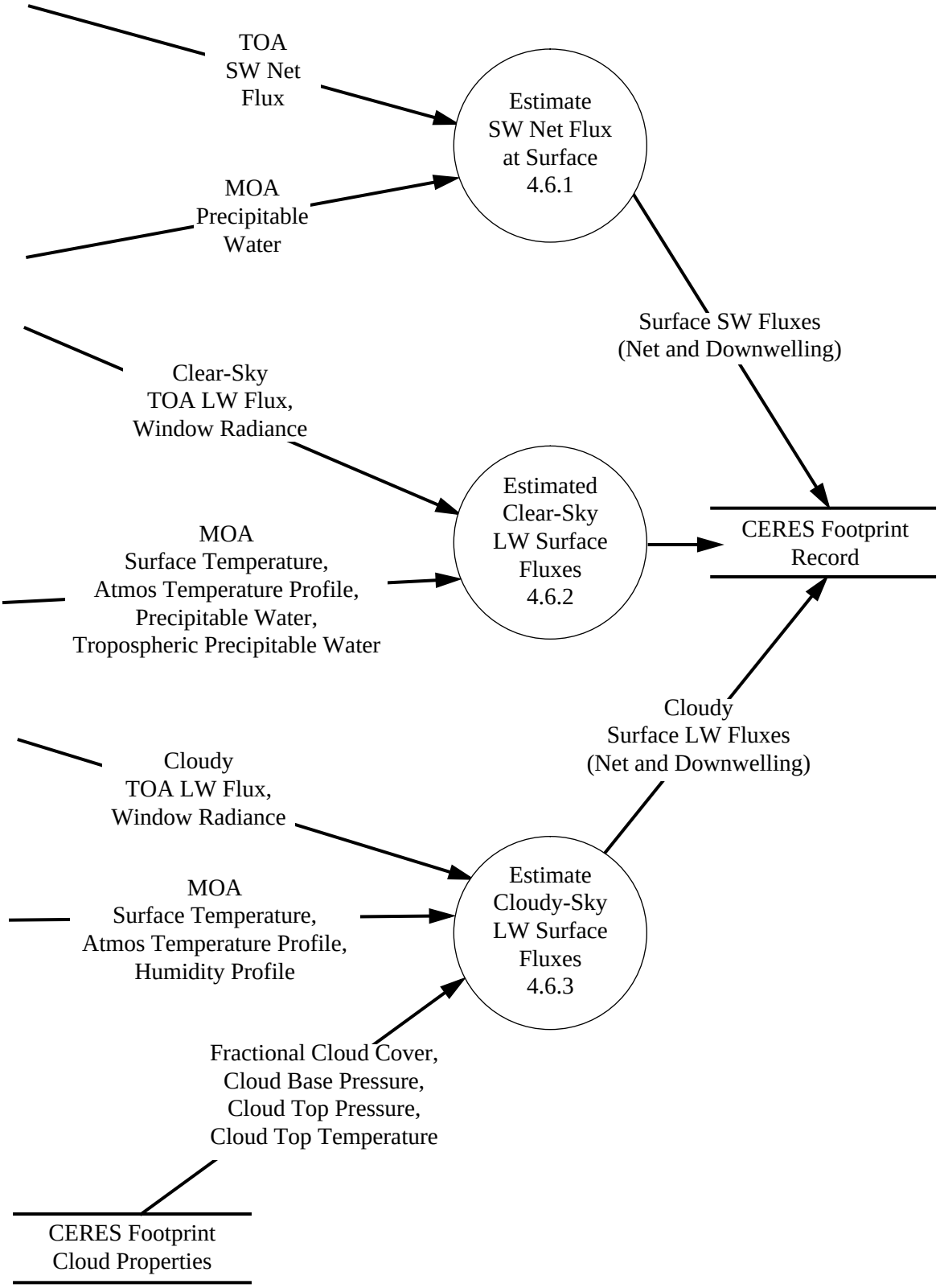

Figure 4.6-1. Major processes for empirical estimation of SW and LW surface radiation budget.

Abstract

This portion of the CERES processing system is intended to produce the shortwave and longwave flux components of the surface radiation budget based on empirical relationships between the CERES TOA fluxes and measured surface radiation budget components. The input to this processing consists of three major kinds of data: CERES footprint cloud properties, CERES TOA fluxes for each footprint, and meteorological data. The output data are the shortwave and longwave flux components at the Earth's surface. There are three kinds of algorithms that we use for this second release of the CERES processing system: net shortwave flux based on the CERES TOA net flux (Li-Leighton), clear-sky longwave fluxes based on relationships derived by Inamdar and Ramanathan, and cloudy-sky longwave fluxes based on relationships derived by Gupta et al.

4.6.0. Empirical Estimates of Shortwave and Longwave Surface Radiation Budget Involving CERES Measurements

4.6.0.1. Introduction

At this point in the CERES processing, we have determined the cloud properties within CERES footprints and we have inverted the CERES radiances to produce TOA fluxes. We also have available the atmospheric constituents and temperatures with modifications that provide what corrections are needed to agree with the basic cloud properties. What we need to do next is to estimate the component fluxes at the Earth's surface.

We often think of these surface radiative fluxes in terms of the two broad spectral bands that we have discussed before: shortwave fluxes and longwave fluxes. Each of these bands have upwelling and downwelling components. Historically, there have been a number of different philosophies regarding the best way to measure the fluxes at the surface and the best way to estimate them from satellite measurements.

In the case of the shortwave fluxes, the classic instrument for measuring the surface flux has been the solar pyranometer, which determines the downwelling flux from all directions. Some observation stations use a shaded pyranometer to measure diffuse flux. An inverted pyranometer can also measure the upwelling flux. However, such instrumentation has difficulties, including thermal convection within the instruments and angular and spectral sensitivities, that make it difficult to accurately characterize it. These problems are compounded by the fact that the angular and spectral radiances emerging from the surface depend both upon the surface properties and upon the radiances coming from the atmosphere. For example, under clear skies the radiance field has a very large value near the Sun's location in the sky and also exhibits considerable limb-brightening in the downwelling diffuse radiance. Blue parts of the shortwave radiance are more diffuse than are the red parts of that spectral band. Given this kind of variability, there have been adherents to measuring the radiance field and integrating radiances to derive fluxes.

The same kind of bifurcation in the measurement community appears in the longwave spectral interval. Here, some measurement devices obtain downwelling fluxes separately from upwelling ones, while other devices obtain the net radiation. Some instruments also measure radiances and use data reduction to produce fluxes.

What is encouraging is the advance of the surface measurement community that is beginning to develop the means for providing reliable surface measurements over at least some portion of the Earth's

surface. Such systems as the Baseline Surface Radiation Network (BSRN) and the measurements from the Atmospheric Radiation Measurement (ARM) program of the Department of Energy offer excellent opportunities to develop empirical relationships between the TOA fluxes from CERES and the surface radiation budget. In this portion of the processing system, we emphasize techniques that use the CERES measurements directly or that have the potential for doing so. In the Surface and Atmospheric Radiation Budget (SARB) portion of the processing, given in ATBD subsystem volume 5.0 and subsidiary volumes, we discuss methods that depend explicitly upon radiative transfer calculations. In the sections below, we discuss the Li-Leighton shortwave calculation and the longwave calculations of Inamdar and Ramanathan, as well as those of Gupta.

4.6.0.2. Shortwave Net Flux at the Surface

The first approximation to the shortwave spectrum's radiative transfer is that it has two spectral subdivisions: a conservative scattering portion that extends from a wavelength of about 0.4 μm to about 0.7 μm, and a completely absorbing portion that covers both the region shortward of 0.4 μm and longward of 0.7 μm. Under this assumption, the net flux at the Earth's surface is related to the net flux at the top of the atmosphere:

$$F_{SFC}^{\uparrow\downarrow} = F_{TOA}^{\uparrow\downarrow} - B \, . \tag{4.6-1}$$

$F^{\uparrow\downarrow}$ represents the net flux at whichever surface we are considering. B represents the solar energy absorbed in the opaque part of the solar spectral range.

In practice, of course, the shortwave radiative transfer is somewhat more complicated. There is ozone absorption across the middle of the "conservative" part of the spectrum, and the near-infrared water vapor bands are not completely black. There are also concerns in the community that clouds are not completely conservative scatterers, as well. Nonetheless, Cess et al. (1991) pursued the possibility of slightly altering the linear relationship between the top of the atmosphere net flux and the surface net flux in the previous equation (4.6-1):

$$F_{SCF}^{\uparrow\downarrow} = AF_{TOA}^{\uparrow\downarrow} - B \, . \tag{4.6-2}$$

If equation (4.6-1) is a reasonable approximation, then equation (4.6-2) should have a value of A that is near 1. Cess et al. (1991) used data from net shortwave radiometers on towers together with instantaneous, simultaneous, and collocated ERBE data to verify that this linear relationship was reasonable. They found that A was about 0.9, and that B was about 50 W-m^{-2}, with each coefficient having a slight dependence on water vapor. Interestingly, the numerical values of A and B were independently derived from a theoretical radiative transfer model and from a regression of the satellite data against the surface net flux measurements. Cess et al. (1991) suggest that the linear relationship appears to be accurate to within about 1%, particularly if the data period extends to a 1-month average to remove some of the noise in the system.

Li and Leighton (1993) extended this simple linear relationship to allow a more accurate inclusion of water vapor and solar zenith angle. They applied this algorithm to the 5-year, global ERBE data set based on the ERBE scanner monthly averages. Li et al. (1993) provide a comparison of this algorithm against a more extensive set of tower measurements of net shortwave flux and direct comparisons with the ERBE data. Their algorithm is discussed in ATBD subsystem 4.6.1.

4.6.0.3. Longwave Fluxes at the Surface

The development of satellite techniques to estimate the longwave radiative fluxes at the Earth's surface has proceeded more slowly. In some ways this problem is more difficult because the downwelling longwave flux responds to both water vapor and to cloud properties. In the tropics, the water vapor is so opaque in the longwave part of the spectrum that most experts believe that clouds are likely to have a

comparatively small positive effect on the downwelling flux. However, this is not the case in other parts of the Earth.

Toward the beginning of the CERES investigation, Ramanathan (Raval and Ramanathan 1989) began pursuing a number of studies related to the greenhouse effect and longwave fluxes at the Earth's surface. They were particularly attracted to the simple picture that longwave radiation escapes nearly unimpeded in the atmospheric window, whereas it is blocked in most of the other parts of the spectrum. The first approximation to the upwelling longwave flux relates this flux directly to the surface temperature, T_{SFC}:

$$F_{LW}^{\uparrow}(SFC) = \sigma T_{SFC}^{4} . \tag{4.6-3}$$

Ramanathan then described the greenhouse effect in terms of the difference

$$G \equiv F_{LW}^{\uparrow}(SFC) - F_{LW}^{\uparrow}(TOA) . \tag{4.6-4}$$

Raval and Ramanathan (1989) ascribed the rapid rise in greenhouse effect to water vapor continuum absorption in the atmospheric window, an effect they called the *super greenhouse effect*. Hallberg and Inamdar (1993) used sensitivity studies to confirm the effect. The confirmation led to the suggestion that variability in the window component of the greenhouse effect could be used as a signature of lower tropospheric water vapor. The absorption of this gas dominates the downward emission at the surface.

In looking for a simple way to obtain the downwelling flux at the surface, Ramanathan began to explore possible relationships between the window flux between 8 μm and 12 μm and the downwelling flux. Further work by Inamdar and Ramanathan (1994) has extended this work. For clear-sky conditions, these explorations led to the algorithm suggested in ATBD subsystem volume 4.6.2. Ramanathan's suggestion also led to the decision by the CERES Science Team to replace the ERBE longwave channel (which was not spectrally flat over the longwave spectral range) with a reasonably flat spectral channel to capture just the window region radiation. Stephens et al. (1994) have independently suggested similar relations that could be used to derive longwave flux at the surface from broadband measurements.

Under cloudy conditions, more work is needed to derive longwave flux at the Earth's surface. In ATBD subsystem volume 4.6.3, Gupta et al. (cf. also Gupta 1989; Gupta et al. 1992; Darnell et al. 1983) provide a description of an algorithm that uses meteorological data from MOA and the cloud properties derived from CERES to compute the longwave fluxes at the Earth's surface.

In figure 4.6-1, we show the decomposition of the three empirically based algorithms for surface flux that we apply in subsystem 4.0. The input and output data for each of these algorithms is not identical, so some care in reading this diagram is needed. In addition, each of these algorithms operates on the data in one CERES footprint. Because of the simplicity of the algorithms, these output fields contribute to both the surface radiation branch of the CERES processing, where these data provide the only source of surface radiation budget data, and in the atmosphere branch of processing. Intercomparison of the two, independently produced, fields will provide an important source of validation and quality control information in the future. The algorithms are described in subsystems 4.6.1, 4.6.2, and 4.6.3.

4.6.0.4. Implementation Issues

There appear to be no major implementation issues at this point. The interfaces between these algorithms and the available data within this subsystem are readily available. The Li-Leighton algorithm uses the CERES TOA fluxes and atmospheric water vapor. The Inamdar-Ramanathan algorithm uses CERES TOA fluxes, the CERES window channel radiance, surface temperature, and precipitable water. The Gupta et al. algorithm uses similar meteorological data, and cloud properties obtained from CERES analysis.

4.6.0.5. Validation plan summary

Output data products are downward and net shortwave surface flux, clear-sky downward longwave ($\lambda > 5.0$ μm), window (8 μm < λ < 12 μm), and non-window surface fluxes, and total-sky downward and net longwave surface fluxes (W-m^{-2}).

The validation criteria are root mean square errors of 20 W-m^{-2} for instantaneous retrievals and 10 W-m^{-2} for gridded monthly averages for both shortwave and longwave surface fluxes.

There are several sources for validation data. A limited validation dataset has been produced from the measurements taken at the ARM/CART Southern Great Plains (SGP) site, and has been made available through the CERES/ARM/GEWEX experiment (CAGEX) at NASA Langley Research Center. The CAGEX database provides measurements taken at the SGP site concerning surface shortwave and longwave fluxes. It is anticipated that collection of high quality surface measurements will continue at the SGP site and will be initiated at the Tropical Western Pacific (TWP) and the North Slope Alaska (NSA) sites. Further data useful for validation should be available through the NOAA Integrated Surface Irradiance Study (ISIS), which utilizes surface fluxes measured by the NOAA Surface Radiation (SURFRAD) network in the U.S. and by the World Climate Research Program (WCRP) Baseline Surface Radiation Network (BSRN) at selected sites around the globe.

The validation of the CERES empirical radiative transfer algorithms will proceed by gathering the necessary input data (simultaneously measured TOA and net surface fluxes for both the shortwave and longwave portions of the spectrum, atmospheric temperature and total column water vapor); applying the radiative transfer algorithms to the measured TOA data to derive simulated surface radiation fluxes which are then compared with the measured surface radiation fluxes; followed by a thorough error analysis to the results of these comparisons. Validation data and results will be made available through anonymous ftp and/or through the World Wide Web.

4.6.0.6. References

Cess, Robert D.; Dutton, Ellsworth, G.; Deluisi, John J.; and Jiang, Feng 1991: Determining Surface Solar Absorption From Broadband Satellite Measurements for Clear Skies—Comparison With Surface Measurements. *J. Climat.*, vol. 4, pp. 236–247.

Darnell, Wayne L.; Gupta, Shashi K.; and Staylor, W. Frank 1983: Downward Longwave Radiation at the Surface From Satellite Measurements. *J. Climat. & Appl. Meteorol.*, vol. 22, no. 11, pp. 1956–1960.

Gupta, Shashi K. 1989: A Parameterization for Longwave Surface Radiation From Sun-Synchronous Satellite Data. *J. Climat.*, vol. 2, pp. 305–320.

Gupta, Shashi K.; Darnell, Wayne L.; and Wilber, Anne C. 1992: A Parameterization for Longwave Surface Radiation From Satellite Data—Recent Improvements. *J. Appl. Meteorol.*, vol. 31, no. 12, pp. 1361–1367.

Hallberg, Robert; and Inamdar, Anand K. 1993: Observations of Seasonal Variations in Atmospheric Greenhouse Trapping and Its Enhancement at High Sea Surface Temperature. *J. Climat.*, vol. 6, no. 5, pp. 920–931.

Inamdar, A. K.; and Ramanathan, V. 1994: Physics of Greenhouse Effect and Convection in Warm Oceans. *J. Climat.*, vol. 7, no. 5, pp. 715–731.

Li, Z.; and Leighton, H. G. 1993: Global Climatologies of Solar Radiation Budgets at the Surface and in the Atmosphere From 5 Years of ERBE Data. *J. Geophys. Res.*, vol. 98, pp. 4919–4930.

Li, Zhanqing; Leighton, H. G.; and Cess, Robert D. 1993: Surface Net Solar Radiation Estimated From Satellite Measurements—Comparisons With Tower Observations. *J. Climat.*, vol. 6, no. 9, pp. 1764–1772.

Raval, A.; and Ramanathan, V. 1989: Observational Determination of the Greenhouse Effect. *Nature*, vol. 342, pp. 758–761.

Stephens, G. L.; Slingo, A.; Webb, M. J.; Jones, A.; and Randall, D. A. 1994: A New Method for Deriving the Atmospheric Greenhouse Effect From Satellite Observations, submitted to *Nature*.

Appendix A

Nomenclature

Acronyms

ADEOS	Advanced Earth Observing System
ADM	Angular Distribution Model
AIRS	Atmospheric Infrared Sounder (EOS-AM)
AMSU	Advanced Microwave Sounding Unit (EOS-PM)
APD	Aerosol Profile Data
APID	Application Identifier
ARESE	ARM Enhanced Shortwave Experiment
ARM	Atmospheric Radiation Measurement
ASOS	Automated Surface Observing Sites
ASTER	Advanced Spaceborne Thermal Emission and Reflection Radiometer
ASTEX	Atlantic Stratocumulus Transition Experiment
ASTR	Atmospheric Structures
ATBD	Algorithm Theoretical Basis Document
AVG	Monthly Regional, Average Radiative Fluxes and Clouds (CERES Archival Data Product)
AVHRR	Advanced Very High Resolution Radiometer
BDS	Bidirectional Scan (CERES Archival Data Product)
BRIE	Best Regional Integral Estimate
BSRN	Baseline Surface Radiation Network
BTD	Brightness Temperature Difference(s)
CCD	Charge Coupled Device
CCSDS	Consultative Committee for Space Data Systems
CEPEX	Central Equatorial Pacific Experiment
CERES	Clouds and the Earth’s Radiant Energy System
CID	Cloud Imager Data
CLAVR	Clouds from AVHRR
CLS	Constrained Least Squares
COPRS	Cloud Optical Property Retrieval System
CPR	Cloud Profiling Radar
CRH	Clear Reflectance, Temperature History (CERES Archival Data Product)
CRS	Single Satellite CERES Footprint, Radiative Fluxes and Clouds (CERES Archival Data Product)
DAAC	Distributed Active Archive Center
DAC	Digital-Analog Converter
DAO	Data Assimilation Office

DB	Database
DFD	Data Flow Diagram
DLF	Downward Longwave Flux
DMSP	Defense Meteorological Satellite Program
EADM	ERBE-Like Albedo Directional Model (CERES Input Data Product)
ECA	Earth Central Angle
ECLIPS	Experimental Cloud Lidar Pilot Study
ECMWF	European Centre for Medium-Range Weather Forecasts
EDDB	ERBE-Like Daily Data Base (CERES Archival Data Product)
EID9	ERBE-Like Internal Data Product 9 (CERES Internal Data Product)
EOS	Earth Observing System
EOSDIS	Earth Observing System Data Information System
EOS-AM	EOS Morning Crossing Mission
EOS-PM	EOS Afternoon Crossing Mission
ENSO	El Niño/Southern Oscillation
ENVISAT	Environmental Satellite
EPHANC	Ephemeris and Ancillary (CERES Input Data Product)
ERB	Earth Radiation Budget
ERBE	Earth Radiation Budget Experiment
ERBS	Earth Radiation Budget Satellite
ESA	European Space Agency
ES4	ERBE-Like S4 Data Product (CERES Archival Data Product)
ES4G	ERBE-Like S4G Data Product (CERES Archival Data Product)
ES8	ERBE-Like S8 Data Product (CERES Archival Data Product)
ES9	ERBE-Like S9 Data Product (CERES Archival Data Product)
FLOP	Floating Point Operation
FIRE	First ISCCP Regional Experiment
FIRE II IFO	First ISCCP Regional Experiment II Intensive Field Observations
FOV	Field of View
FSW	Hourly Gridded Single Satellite Fluxes and Clouds (CERES Archival Data Product)
FTM	Functional Test Model
GAC	Global Area Coverage (AVHRR data mode)
GAP	Gridded Atmospheric Product (CERES Input Data Product)
GCIP	GEWEX Continental-Phase International Project
GCM	General Circulation Model
GEBA	Global Energy Balance Archive
GEO	ISSCP Radiances (CERES Input Data Product)
GEWEX	Global Energy and Water Cycle Experiment

GLAS	Geoscience Laser Altimetry System
GMS	Geostationary Meteorological Satellite
GOES	Geostationary Operational Environmental Satellite
HBTM	Hybrid Bispectral Threshold Method
HIRS	High-Resolution Infrared Radiation Sounder
HIS	High-Resolution Interferometer Sounder
ICM	Internal Calibration Module
ICRCCM	Intercomparison of Radiation Codes in Climate Models
ID	Identification
IEEE	Institute of Electrical and Electronics Engineers
IES	Instrument Earth Scans (CERES Internal Data Product)
IFO	Intensive Field Observation
INSAT	Indian Satellite
IOP	Intensive Observing Period
IR	Infrared
IRIS	Infrared Interferometer Spectrometer
ISCCP	International Satellite Cloud Climatology Project
ISS	Integrated Sounding System
IWP	Ice Water Path
LAC	Local Area Coverage (AVHRR data mode)
LaRC	Langley Research Center
LBC	Laser Beam Ceilometer
LBTM	Layer Bispectral Threshold Method
Lidar	Light Detection and Ranging
LITE	Lidar In-Space Technology Experiment
Lowtran 7	Low-Resolution Transmittance (Radiative Transfer Code)
LW	Longwave
LWP	Liquid Water Path
MAM	Mirror Attenuator Mosaic
MC	Mostly Cloudy
MCR	Microwave Cloud Radiometer
METEOSAT	Meteorological Operational Satellite (European)
METSAT	Meteorological Satellite
MFLOP	Million FLOP
MIMR	Multifrequency Imaging Microwave Radiometer
MISR	Multiangle Imaging Spectroradiometer
MLE	Maximum Likelihood Estimate
MOA	Meteorology Ozone and Aerosol
MODIS	Moderate-Resolution Imaging Spectroradiometer

MSMR	Multispectral, multiresolution
MTSA	Monthly Time and Space Averaging
MWH	Microwave Humidity
MWP	Microwave Water Path
NASA	National Aeronautics and Space Administration
NCAR	National Center for Atmospheric Research
NCEP	National Centers for Environmental Prediction
NESDIS	National Environmental Satellite, Data, and Information Service
NIR	Near Infrared
NMC	National Meteorological Center
NOAA	National Oceanic and Atmospheric Administration
NWP	Numerical Weather Prediction
OLR	Outgoing Longwave Radiation
OPD	Ozone Profile Data (CERES Input Data Product)
OV	Overcast
PC	Partly Cloudy
POLDER	Polarization of Directionality of Earth's Reflectances
PRT	Platinum Resistance Thermometer
PSF	Point Spread Function
PW	Precipitable Water
RAPS	Rotating Azimuth Plane Scan
RPM	Radiance Pairs Method
RTM	Radiometer Test Model
SAB	Sorting by Angular Bins
SAGE	Stratospheric Aerosol and Gas Experiment
SARB	Surface and Atmospheric Radiation Budget Working Group
SDCD	Solar Distance Correction and Declination
SFC	Hourly Gridded Single Satellite TOA and Surface Fluxes (CERES Archival Data Product)
SHEBA	Surface Heat Budget in the Arctic
SPECTRE	Spectral Radiance Experiment
SRB	Surface Radiation Budget
SRBAVG	Surface Radiation Budget Average (CERES Archival Data Product)
SSF	Single Satellite CERES Footprint TOA and Surface Fluxes, Clouds
SSMI	Special Sensor Microwave Imager
SST	Sea Surface Temperature
SURFMAP	Surface Properties and Maps (CERES Input Product)
SW	Shortwave
SWICS	Shortwave Internal Calibration Source

SYN	Synoptic Radiative Fluxes and Clouds (CERES Archival Data Product)
SZA	Solar Zenith Angle
THIR	Temperature/Humidity Infrared Radiometer (Nimbus)
TIROS	Television Infrared Observation Satellite
TISA	Time Interpolation and Spatial Averaging Working Group
TMI	TRMM Microwave Imager
TOA	Top of the Atmosphere
TOGA	Tropical Ocean Global Atmosphere
TOMS	Total Ozone Mapping Spectrometer
TOVS	TIROS Operational Vertical Sounder
TRMM	Tropical Rainfall Measuring Mission
TSA	Time-Space Averaging
UAV	Unmanned Aerospace Vehicle
UT	Universal Time
UTC	Universal Time Code
VAS	VISSR Atmospheric Sounder (GOES)
VIRS	Visible Infrared Scanner
VISSR	Visible and Infrared Spin Scan Radiometer
WCRP	World Climate Research Program
WG	Working Group
Win	Window
WN	Window
WMO	World Meteorological Organization
ZAVG	Monthly Zonal and Global Average Radiative Fluxes and Clouds (CERES Archival Data Product)

Symbols

A	atmospheric absorptance
$B_\lambda(T)$	Planck function
C	cloud fractional area coverage
CF_2Cl_2	dichlorofluorocarbon
$CFCl_3$	trichlorofluorocarbon
CH_4	methane
CO_2	carbon dioxide
D	total number of days in the month
D_e	cloud particle equivalent diameter (for ice clouds)
E_o	solar constant or solar irradiance
F	flux
f	fraction

G_a	atmospheric greenhouse effect
g	cloud asymmetry parameter
H_2O	water vapor
I	radiance
i	scene type
m_i	imaginary refractive index
$\hat{N}$	angular momentum vector
N_2O	nitrous oxide
O_3	ozone
P	point spread function
p	pressure
Q_a	absorption efficiency
Q_e	extinction efficiency
Q_s	scattering efficiency
R	anisotropic reflectance factor
r_E	radius of the Earth
r_e	effective cloud droplet radius (for water clouds)
r_h	column-averaged relative humidity
S_o	summed solar incident SW flux
S_o'	integrated solar incident SW flux
T	temperature
T_B	blackbody temperature
t	time or transmittance
W_{liq}	liquid water path
w	precipitable water
$\hat{x}_o$	satellite position at t_o
x, y, z	satellite position vector components
$\dot{x}, \dot{y}, \dot{z}$	satellite velocity vector components
z	altitude
z_{top}	altitude at top of atmosphere
α	albedo or cone angle
β	cross-scan angle
γ	Earth central angle
γ_{at}	along-track angle
γ_{ct}	cross-track angle
δ	along-scan angle
ε	emittance
Θ	colatitude of satellite
θ	viewing zenith angle

θ_o	solar zenith angle
λ	wavelength
μ	viewing zenith angle cosine
μ_o	solar zenith angle cosine
ν	wave number
ρ	bidirectional reflectance
τ	optical depth
$\tau_{aer}(p)$	spectral optical depth profiles of aerosols
$\tau_{H_2O\lambda}(p)$	spectral optical depth profiles of water vapor
$\tau_{O_3}(p)$	spectral optical depth profiles of ozone
Φ	longitude of satellite
ϕ	azimuth angle
$\tilde{\omega}_o$	single-scattering albedo

Subscripts:

c	cloud
cb	cloud base
ce	cloud effective
cld	cloud
cs	clear sky
ct	cloud top
ice	ice water
lc	lower cloud
liq	liquid water
s	surface
uc	upper cloud
λ	spectral wavelength

Units

AU	astronomical unit
cm	centimeter
cm-sec^{-1}	centimeter per second
count	count
day	day, Julian date
deg	degree
deg-sec^{-1}	degree per second
DU	Dobson unit
erg-sec^{-1}	erg per second
fraction	fraction (range of 0–1)
g	gram

$g\text{-}cm^{-2}$	gram per square centimeter
$g\text{-}g^{-1}$	gram per gram
$g\text{-}m^{-2}$	gram per square meter
h	hour
hPa	hectopascal
K	Kelvin
kg	kilogram
$kg\text{-}m^{-2}$	kilogram per square meter
km	kilometer
$km\text{-}sec^{-1}$	kilometer per second
m	meter
mm	millimeter
μm	micrometer, micron
N/A	not applicable, none, unitless, dimensionless
$ohm\text{-}cm^{-1}$	ohm per centimeter
percent	percent (range of 0–100)
rad	radian
$rad\text{-}sec^{-1}$	radian per second
sec	second
sr^{-1}	per steradian
W	watt
$W\text{-}m^{-2}$	watt per square meter
$W\text{-}m^{-2}sr^{-1}$	watt per square meter per steradian
$W\text{-}m^{-2}sr^{-1}\mu m^{-1}$	watt per square meter per steradian per micrometer